

Exploring Optical Sensing Mechanisms in Metal Halide Perovskites for Hydrogen Gas Detection

Jorge Arteaga and Sayantani Ghosh*

Metal halide perovskites (MHPs) are emerging as promising candidates for gas sensing due to their tunable optoelectronic properties, room temperature operation, and scalable fabrication. In this work, hydrogen (H₂) sensing capabilities of methylammonium lead iodide (MAPI) thin films via photoluminescence (PL) spectroscopy is investigated. MAPI films demonstrate a consistent and rapid PL intensity response in a matter of seconds upon exposure to H₂, characterized by an initial increase followed by a decay below baseline, which recovers in ambient air. This reversible behavior is preserved over multiple cycles over an hour, indicating reusability. The magnitude and duration of the PL response vary with H₂ concentration, demonstrating the sensor's ability to detect not only presence but also quantity of gas. Control experiments using encapsulated films confirm specificity to H₂, and X-ray Diffraction (XRD) analysis confirm the interaction does not cause any significant crystallographic changes. Further analysis with thinner films and mixed-halide compositions suggests that both surface and bulk interactions, as well as defect-mediated processes, contribute to sensing. This study establishes MAPI as a viable optical sensor for H₂ gas with fast response, sensitivity to concentration, and potential for low-cost implementation.

sources like solar or wind,^[3–5] which further helps reduce dependence on fossil fuels and supports global efforts to cut greenhouse gas emissions.^[6]

Despite these advantages H₂ poses significant safety challenges. It is odorless, colorless, and highly flammable,^[7,8] with a broad explosive range (4%–75% in air) and extremely low ignition energy (0.02 mJ).^[8] H₂ is typically stored and transported in one of three forms: compressed gas, cryogenic liquid, or chemically bound in materials such as metal hydrides.^[4] Compressed hydrogen is stored under high pressure (typically 350–700 bar), while cryogenic hydrogen is liquefied at extremely low temperatures (–253 °C).^[9] These methods, especially under high pressure or extreme cold, add complexity to system design and increase the risk of leaks due to material degradation, microcracks, or seal failures.^[10] Additionally, its small molecular size allows it to diffuse through many common materials,^[11] further exacerbating the risk of undetected

1. Introduction

Hydrogen (H₂) is a versatile energy carrier capable of storing, transporting, and delivering energy cleanly,^[1–3] emitting only water upon combustion or electrochemical conversion.^[3] Due to its potential to decarbonize multiple sectors ranging from industrial processes to transportation and power generation, H₂ is a cornerstone of future sustainable energy systems.^[4] Additionally, hydrogen can be produced via electrolysis powered by renewable

leakage. These storage and transportation conditions amplify the need for sensitive, rapid, and reliable detection technologies. Conventional sensors such as thermal or electrochemical ones can face challenges, which include slow response under low concentrations, high power consumption, or instability in extreme environments (e.g., cold temperatures, high humidity, or variable pressure).^[11] Furthermore, in applications like fuel cell vehicles or aerospace systems, real-time and localized sensing is critical,^[12] and room-temperature optical sensors likely offer safer and more adaptable alternatives.

Metal halide perovskites (MHPs) have an ABX₃ crystal structure, where A is a monovalent cation, commonly methylammonium (MA), formamidinium (FA), or cesium (Cs), B is a bivalent cation such as lead (Pb) or tin (Sn), and X is a halide (Cl[–], Br[–], or I[–]).^[13–20] MHPs possess exceptional optoelectronic properties such as high absorption coefficients,^[15] tunable bandgaps,^[16] and long carrier diffusion lengths.^[17] Originally studied for photovoltaic and light-emitting applications,^[18–20] MHPs are now being explored as gas sensors^[21–27] due to their defect-sensitive photoluminescence (PL), ambient operation, and facile solution-processable fabrication. Recent work has demonstrated the viability of MHPs in detecting a variety of analytes. MAPbBr₃ single crystals^[21,22] and CsPbBr₃ quantum dots^[23] have been used

J. Arteaga, S. Ghosh
Department of Physics
School of Natural Science
University of California
Merced, CA 95343, USA
E-mail: sghosh@ucmerced.edu

 The ORCID identification number(s) for the author(s) of this article can be found under <https://doi.org/10.1002/adsr.202500078>

© 2025 The Author(s). Advanced Sensor Research published by Wiley-VCH GmbH. This is an open access article under the terms of the [Creative Commons Attribution](https://creativecommons.org/licenses/by/4.0/) License, which permits use, distribution and reproduction in any medium, provided the original work is properly cited.

DOI: 10.1002/adsr.202500078

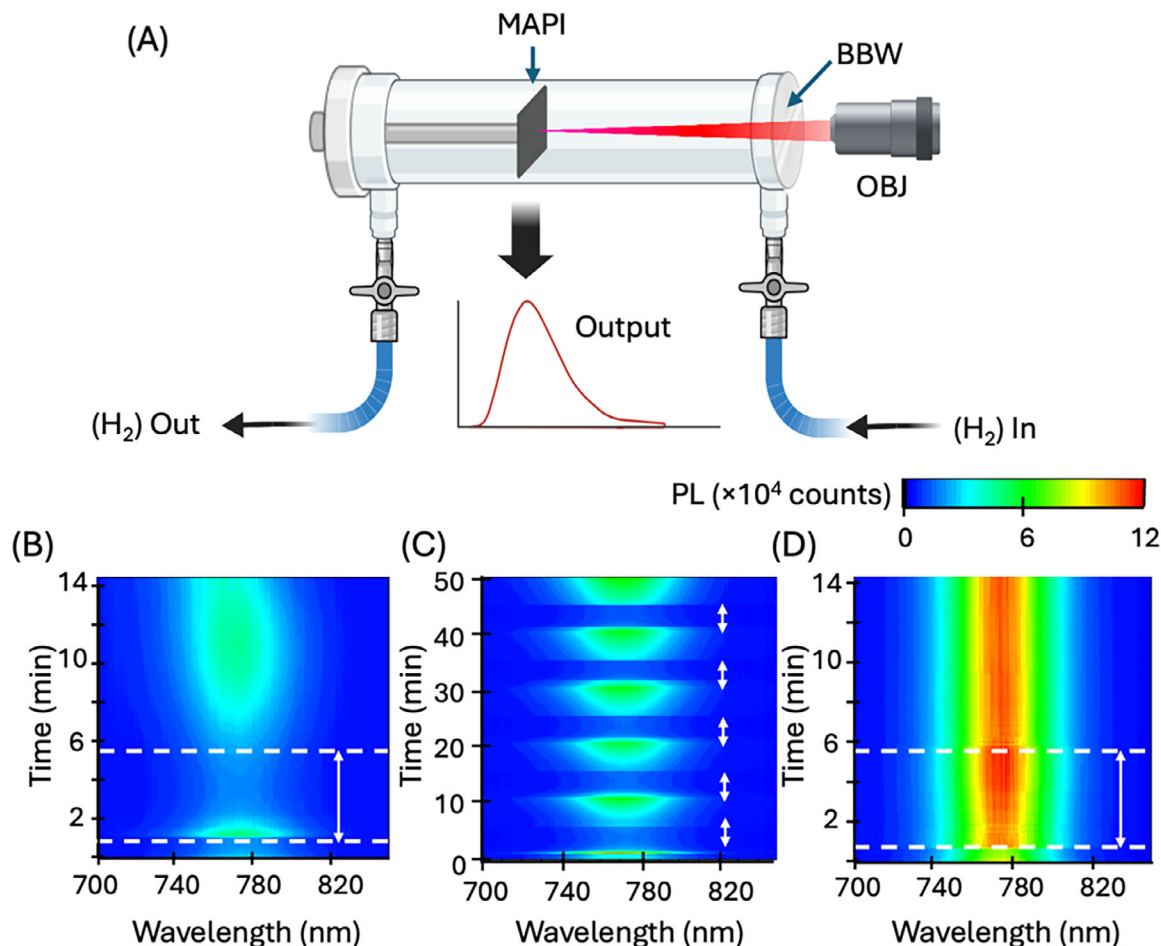


Figure 1. A) Schematic of experimental set up. BBW: Broadband window; MAPI: sample film; OBJ: Objective. B) PL intensity as a function of emission wavelength and time for unencapsulated MAPI thin film. Duration of H₂ exposure is indicated by the dashed lines and double-headed arrows. C) Unencapsulated MAPI film intensity tracked with repeated H₂ exposure over 50 min. D) Control measurement using an encapsulated MAPI film. Duration of H₂ exposure is indicated by the dashed lines and double-headed arrows.

to optically detect ammonia (NH₃), while MAPbI₃ films have exhibited chemiresistive behavior in the presence of NO₂.^[24] Mixed halide and double perovskites such as CsBiAgBr₆ have been applied in humidity sensing,^[25] leveraging changes in resistivity. These findings underscore the materials' flexibility and potential for chemical tuning to improve selectivity and sensitivity. In the context of hydrogen detection, most studies involving MHPs have focused on electrical sensing modalities, such as the use of mixed-conducting perovskite oxides for electrochemical hydrogen detection in solid-state sensor platforms,^[26] and the demonstration of chemiresistive hydrogen sensors based on halide perovskite films,^[27] which exhibit measurable conductivity changes upon gas exposure. These systems, while promising, typically operate in environments requiring precise voltage control and may suffer from long-term stability challenges due to ion migration^[28] and environmental degradation.^[29] Optical sensing offers several advantages, including contactless measurement, ambient operation, and immunity to electromagnetic interference,^[30] making it especially attractive for applications in aerospace, automotive fuel systems, and cryogenic hydrogen storage,^[12] where non-intrusive and rapid detection is critical.

This work addresses this gap by demonstrating that MAPI thin films exhibit a distinct and repeatable PL response when exposed to H₂ gas, highlighting the potential of perovskite-based materials as reusable, room-temperature optical sensors capable of detecting hydrogen presence and concentration with high temporal resolution.

2. Results and Discussion

MAPI thin films were fabricated via spin coating and annealing following established procedures,^[31] detailed in the Experimental Section. Data in the following sections are acquired from MAPI films annealed at 90 °C. **Figure 1A** illustrates the experimental setup used to study the optical response of the thin films upon exposure to H₂. The sample (MAPI) is mounted inside a customized gas flow cell, with a transparent broadband window (BBW) to allow for optical access. A collimated light source, directed through an objective (OBJ), excites the MAPI film, and the resulting PL emission is collected in reflection and recorded as the output signal. Hydrogen gas is introduced from the front end of the chamber ("H₂ In") at the rate of 3 L min⁻¹, which al-

lows us to fill the gas chamber in 18 s, and is allowed to exit from the back (“H₂ Out”). This design allows real-time monitoring of the PL response under controlled H₂ flow conditions.

2.1. Reversible PL Response to H₂ Exposure

Figure 1B tracks PL emission spectra of a MAPI film over time, and the period between the dashed lines (also indicated by the double-headed arrow) is when the flow cell is filled with H₂. The sample showed a spike in PL emission intensity that quickly tapered off to below the initial value. Upon releasing H₂, the PL emission intensity recovered. To determine the repeatability of the response, we cycled between H₂ and ambient air at 5 min intervals, as shown in Figure 1C. The noted response of MAPI to H₂ was repeated each cycle, with an initial spike in emission intensity that quickly decayed. The behavior during periods without H₂ flow was also consistent, with the emission intensity recovering back to the initial intensity. This behavior is also observed in MAPI films annealed at other temperatures (Figure S1, Supporting Information). For control, we repeated the measurements with a MAPI film that had been encapsulated in Dow-Corning space-grade encapsulant DC 93–500, a low outgassing silicone elastomer typically used to encapsulate electronics in aerospace applications. As seen in Figure 1D, the encapsulated MAPI film produced no response to the introduction of H₂ gas, confirming that the intensity change seen before is caused by the H₂ interacting with MAPI and is not simply the result of a shift in alignment caused by gas flow.

To further test the repeatability, we cycled H₂ and ambient air flow at 1 min intervals for 10 cycles in Figure 2A, followed by an hour’s gap, when the film was left in ambient air, before repeating the measurement for another 5 cycles. The same response was seen, although after the break, the starting emission intensity for each cycle was beginning to reduce. We plot the integrated PL intensity with time in Figure 2B where the shaded regions indicate H₂ presence and observe that the PL intensity exhibits a distinctive rise-and-fall profile. A more detailed look at the nature of this response in the inset reveals that the PL increases almost immediately when H₂ flow is initiated. This suggests a fast interaction between H₂ molecules and the MAPI film surface, likely via adsorption, and indicates that surface states or shallow trap passivation may be involved, briefly enhancing radiative recombination.^[32,33] This increase is not persistent and tapers off to a level below the original baseline. This decay happens over tens of seconds and appears to stabilize before the end of the 1 min exposure window, which suggests that continued exposure leads to deeper interactions between H₂ and the film, likely penetration into the bulk, or interaction with deeper trap states. While we tentatively attribute these trap states to iodide vacancies based on prior literature^[34,35] and the suppressed PL response observed in mixed-halide films (Figure S3, Supporting Information), conclusive identification of the underlying defects would require additional techniques such as XPS, EPR, or DFT modeling, which are outside the scope of this optical study. These interactions likely enhance non-radiative recombination, leading to a net PL quenching effect. Once H₂ flow is stopped and ambient air is reintroduced, the PL intensity gradually returns to baseline, completing a reversible cycle.

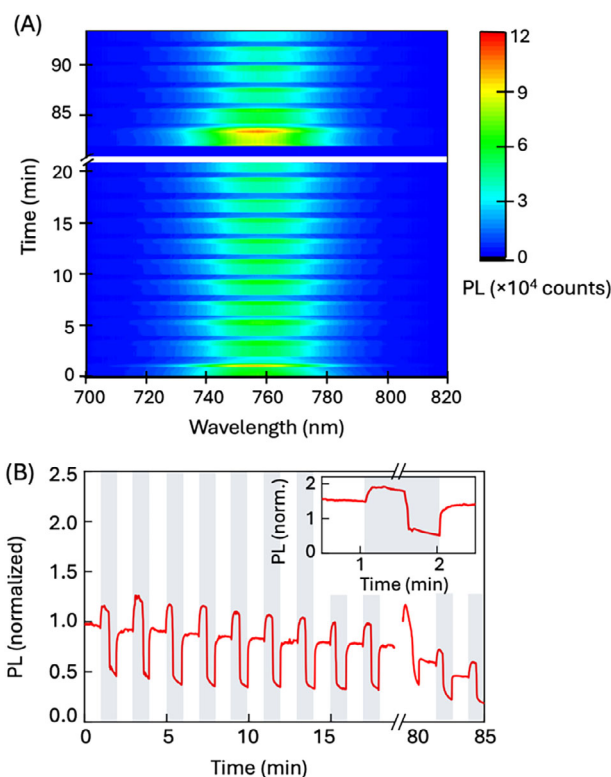


Figure 2. A) PL map of H₂ cycling on and off in 1 min intervals, followed by a 1 h break and resumption of measurements. B) Integrated PL intensity plotted with time. *Inset:* Details of PL profile over one cycle.

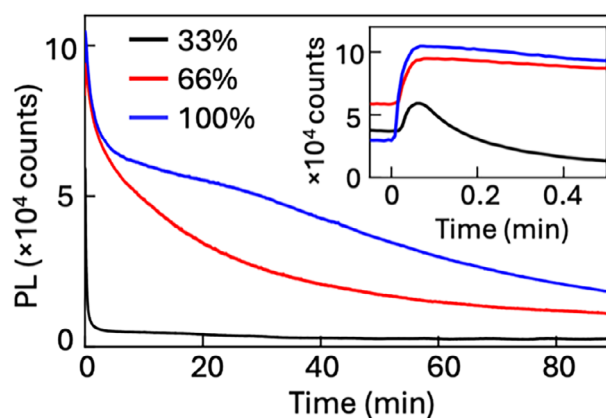


Figure 3. PL intensity for MAPI exposed to H₂-N₂ gas mixture for the entire interval starting at 0 min, for different proportions of H₂. *Inset:* Same data highlighting the first 0.5 min when gas flow begins.

2.2. Concentration-Dependent Sensing Behavior

To evaluate the sensitivity of MAPI thin films to varying concentrations of H₂ gas, we performed a series of measurements under controlled exposure to H₂ diluted in N₂. The gas flow cell was flushed and then filled with gas mixtures containing different volume percentages of hydrogen in nitrogen, and the PL response recorded over an hour, going beyond the transient measurements performed so far. As shown in Figure 3, the PL intensity exhibits

a clear, concentration-dependent response. Upon the introduction of each gas mixture at time “0”, the PL intensity increases as expected with the peak magnitude scaling with hydrogen concentration, discernible more clearly in the inset to Figure 3. Notably, higher concentrations of H₂ produce a more prolonged initial PL enhancement. Following this increase, the PL intensity decays gradually toward a new steady-state level as the flow cell remains sealed. The rate and extent of this decay are also concentration dependent, with higher concentrations lead to slower decay kinetics and a higher final PL baseline. With this concentration-scaling behavior in the inset, we demonstrate that MAPI thin films can serve as optical hydrogen sensors capable of detecting not only the presence of H₂ but also providing a quantitative estimate of its concentration, all while operating at room temperature and without rapid irreversible degradation.

The dynamics of the PL intensity response upon hydrogen exposure reveal clear concentration-dependent trends that offer further insight into the sensing mechanism. For all tested concentrations, PL reaches its peak within 4 s of gas exposure, indicating a rapid onset of interaction, likely via surface adsorption. The magnitude of the PL peak increases systematically with concentration, doubling between the lowest and highest H₂ concentrations, consistent with a higher density of accessible interaction sites or greater trap filling at elevated gas levels. The subsequent decay behavior, analyzed using bi-exponential fits, reveals two distinct pathways (Table S1, Supporting Information): a fast decay component likely associated with shallow traps, and a slower decay that reflects deeper or more persistent interactions. At 33% an amplitude-weighted average lifetime of 1.5 min. As the hydrogen concentration increases, both components lengthen substantially, with average lifetimes of 16 min at 66% H₂ and nearly 100 min at 100% H₂. Together, these results support a biphasic sensing mechanism in which the initial, reversible PL enhancement is followed by a slower, dose-dependent evolution of recombination dynamics. To estimate the limit of detection (LOD) for this sensor under our current optical configuration, we applied the standard $3\sigma/S$ criterion, where σ is the standard deviation of the baseline (air-only) signal and S is the sensitivity at low H₂ concentrations. Using the 33% H₂ dataset, we obtained a baseline noise of ≈ 12664 counts and a sensitivity of ≈ 1341 counts per % H₂, yielding an LOD of $\approx 28.3\%$ H₂. While this value reflects strong modulation at higher concentrations, the optical readout could be further optimized to improve low-dose detection, for example via signal averaging, lock-in detection, or pre-concentration approaches.

Hydrogen gas sensors employ^[1,12] a variety of mechanisms, including catalytic, electrochemical, resistive, and mechanical. Each have their unique advantages and limitations. Catalytic sensors detect the heat released from H₂ oxidation on a catalyst surface and are known for their robustness and simplicity,^[36] though they typically exhibit slow response times (≈ 8 s) and poor selectivity, particularly to carbon monoxide and other combustible gases.^[37] Electrochemical sensors, which rely on charge transport changes at an electrode, can detect concentrations down to 40 ppm and operate at low power.^[38] However, their narrow temperature range and cross-sensitivity to other gases can be limiting.^[39] Resistive sensors using semiconducting metal oxides are valued for their high sensitivity (down to 10 ppm) and fast response times (4–20 s^[12,40]), but they require high operat-

ing temperatures (180–450 °C^[41]) and are vulnerable to humidity and pressure variations.^[42,43] Mechanical sensors, which exploit volume changes in materials upon H₂ uptake (e.g., lattice expansion in palladium), are advantageous for use in explosive environments due to their passive operation,^[44] but typically suffer from long response times (> 90 s,^[45]). In contrast, the MAPI-based optical sensor developed in this study operates at room temperature, is contactless and bias-free, and shows a distinct photoluminescence response within seconds of H₂ exposure. While its current detection limit ($\approx 28\%$ H₂) is higher than many commercial alternatives, its rapid reversibility, structural stability, and potential for miniaturization and remote sensing make it a compelling platform for applications such as cryogenic storage and aerospace systems, where fast, low-power, non-intrusive monitoring is critical.

2.3. Spatial Inhomogeneity and Persistent Optical Effects

The concentration dependent data additionally highlighted the longevity of PL change driven by continued exposure to H₂. To investigate further, we performed spatially resolved PL mapping to assess how H₂ exposure affects other spectral aspects, including both the emission peak wavelength and the recombination lifetimes, before, during, and after H₂ exposure. Additionally, in contrast to the rapid-scan data in Figure 1 and Figure 2, these spatial maps are acquired over a longer time interval (≈ 25 min each) and represent quasi-steady-state snapshots during each condition. It is important to note that the measurements in Figure 2 and Figure 3 reflect continuous time-dependent photoluminescence (PL) intensity tracking under constant illumination, not time-resolved photoluminescence spectroscopy (TRPL). These experiments monitor changes in the steady-state emission intensity as a function of hydrogen exposure time. In contrast, TRPL measurements discussed later (Section 2.3) use pulsed excitation to extract carrier recombination lifetimes. While both methods are time-resolved in different senses, they probe distinct aspects of the system: PL tracking reveals dynamic optical responses to environmental changes, whereas TRPL provides insight into intrinsic recombination kinetics. Figure 4A–C display 2D maps of the emission intensity, peak wavelength (λ) and charge carrier lifetime (τ), respectively, measured across the same area of the film at each of the three timepoints. Figure 4D–F provide statistical boxplots summarizing the spatial distributions of the data in these maps. The emission intensity and λ are extracted from PL spectra, while τ is calculated from TRPL curves (Figure S3, Supporting Information) fit with bi-exponential decay functions $I_{PL} = A_1 \exp(-t/\tau_1) + A_2 \exp(-t/\tau_2)$, where τ_1 and τ_2 are the fast and slow time scales, respectively, representing two different routes for recombination.^[46] From the fit, an average lifetime τ is calculated as follows: $\tau = A_1 \tau_1^2 + A_2 \tau_2^2 / (A_1 \tau_1 + A_2 \tau_2)$. Upon H₂ exposure, the PL maps show a modest increase in emission intensity, a consistent blueshift in peak wavelength (λ), and a rise in lifetime (τ), all distributed heterogeneously across the scanned area. Notably, none of these parameters return to baseline after re-exposure to ambient air, indicating that hydrogen induces semi-persistent changes. These maps, acquired more slowly than prior measurements, reflect the equilibrated optical state and confirm shifts in median values and broadened distributions.

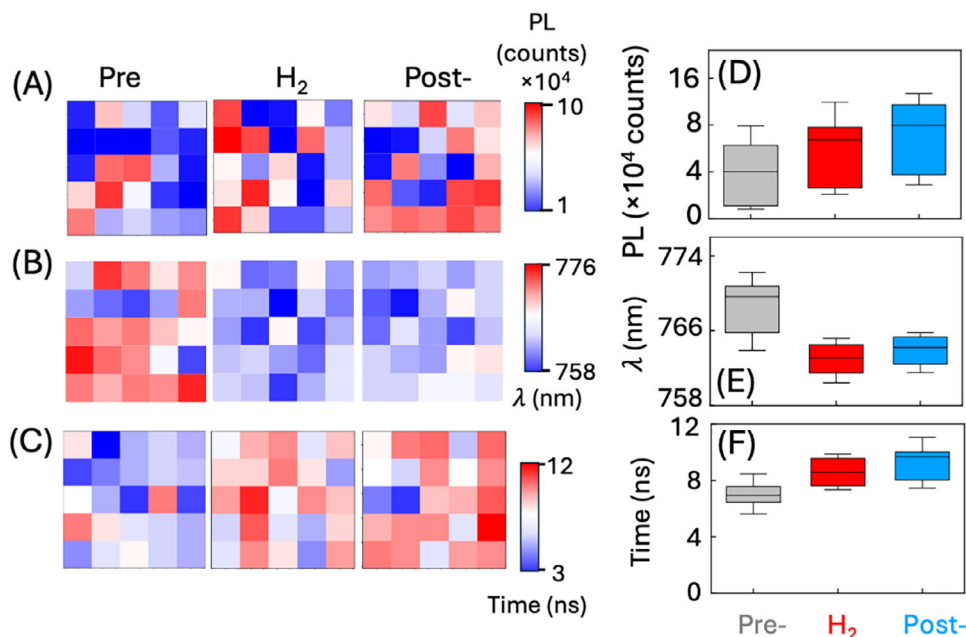


Figure 4. Spatially-resolved PL maps of a MAPI sample over the same $1.5 \times 1.5 \text{ mm}^2$ area before (pre), during and after H_2 exposure, showing the A) emission intensity, B) peak emission wavelengths (λ) and C) recombination lifetimes. The data distribution from these maps displayed in D–F) where the whiskers indicate one standard deviation, and the horizontal lines are the median values.

In particular, the recombination lifetime component τ_2 extracted from TRPL data increases noticeably upon hydrogen exposure and does not fully return to baseline even after ambient recovery. Since τ_2 is typically associated with trap-assisted recombination,^[46–48] this increase suggests that H_2 interacts with deeper trap states, potentially by diffusing into the bulk and altering defect distributions. In contrast, τ_1 remains largely unchanged, indicating that shallow trap-mediated recombination is less affected by prolonged H_2 presence. These observations reinforce the biphasic sensing mechanism inferred from steady-state PL behavior (Figure 3), which indicate a rapid passivation of shallow traps at the surface, followed by slower hydrogen interaction with bulk or deep-level defects. In MHPs, shallow trap states are typically associated with surface defects or halide vacancies located near the conduction or valence band edges.^[46–48] These traps can transiently capture carriers but are often passivated by adsorbed molecules such as hydrogen, leading to reversible PL enhancement. In contrast, deeper trap states lie farther from the band edges and are more strongly associated with long-lived non-radiative recombination. These may arise from bulk defects, undercoordinated ions, or degradation byproducts.^[49] The fast and slow decay components observed in our TRPL data (τ_1 and τ_2 , respectively) are interpreted as signatures of these two distinct trap populations.

In Figure 5 we track the evolution of the recombination lifetime of a MAPI film over 3 h of monitoring, where the lifetimes are extracted from TRPL maps over $1.5 \times 1.5 \text{ mm}^2$ of the film. The gray box indicates lifetimes of the film prior to H_2 exposure, red ones correspond to intervals when the chamber is filled with H_2 and sealed, while the blue boxes represent periods under ambient air after H_2 is released. There is a clear enhancement of recombination times initially as MAPI is exposed to H_2 but by

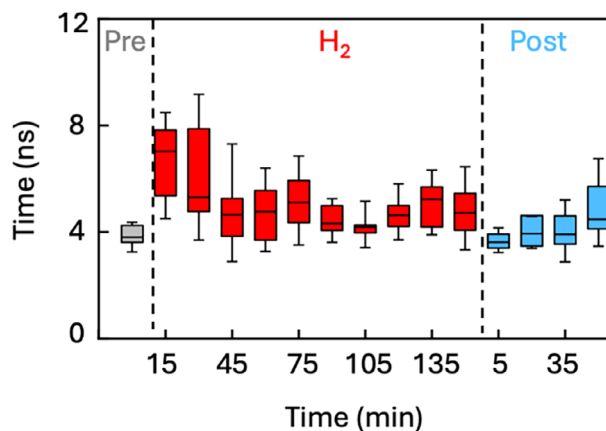


Figure 5. Recombination lifetime data obtained from PL maps before (pre), during and after H_2 exposure, when the exposure period is two hours. The whiskers indicate one standard deviation, and the horizontal lines are the median values.

90 min during the same interval the median lifetime is close to the pre-exposure value, and persists there once H_2 is released. While Figures 2 and 4 demonstrate reversible PL modulation over short cycles, longer exposure studies reveal partial persistence in both PL intensity and carrier lifetimes. Notably, the median lifetime increases during hydrogen exposure in Figure 5, but returns close to the baseline only after 90 min, suggesting delayed equilibration. Furthermore, the steady decline in baseline PL intensity observed in repeated cycling (Figure 2B) suggests cumulative effects, potentially due to progressive trap formation

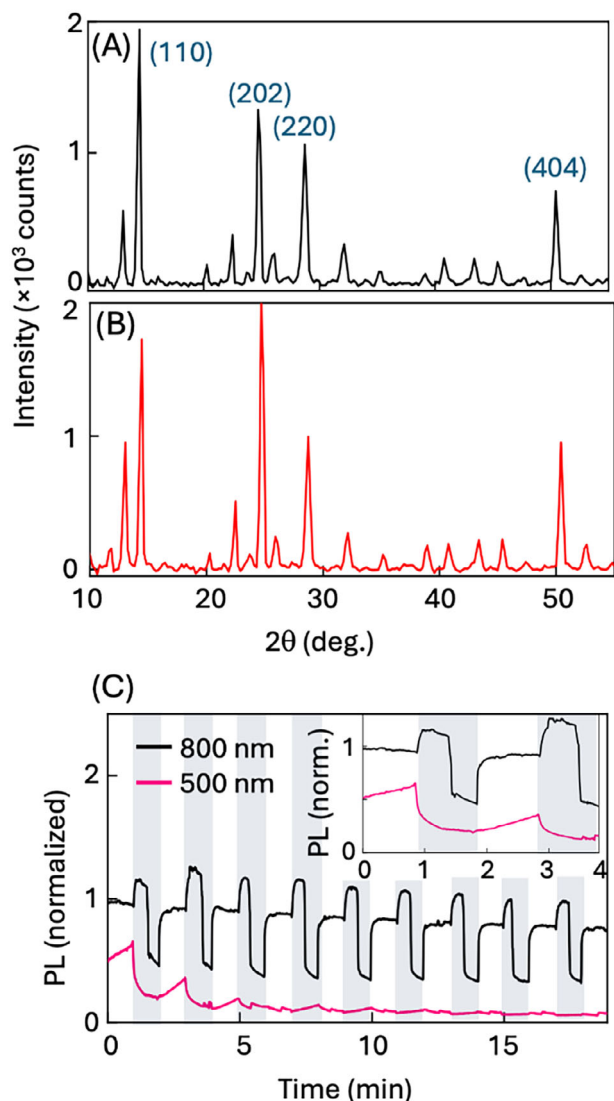


Figure 6. XRD data A) before and B) after H_2 exposure. C) Comparison of PL emission intensities for two MAPI films of different thicknesses. (inset) PL profile enlarged over first two H_2 cycles.

or redistribution. These results point to incomplete reversibility, especially in the deeper trap population reflected by τ_2 .

2.4. Crystallographic Robustness and Film Thickness Dependence

While the spatial PL maps indicate hydrogen-induced modulation of optical properties across the film, we next turn to structural characterization to assess whether these changes are accompanied by any permanent alterations to the crystallographic framework. We conducted X-ray diffraction (XRD) measurements before and after H_2 exposure, as shown in **Figure 6A,B**, respectively. The diffraction patterns in both display the expected peaks of the tetragonal MAPI phase, with no observable peak shifts, broadening, or emergence of new reflections, confirming that the crystal structure remains intact, and that H_2 exposure

does not induce decomposition or phase transitions. To evaluate whether strain might contribute to the observed PL blueshift in **Figure 5B,E**, we calculated the lattice parameters using the (110) and (202) reflections. The extracted values for the exposed film ($a = b = 0.8674$ nm and $c = 1.2975$ nm) are consistent with the unexposed sample and reported values for tetragonal MAPI.^[50] The absence of measurable peak shifts indicates that lattice expansion does not play a significant role, and that the blueshift is more likely due to surface defect passivation or electronic redistribution. However, a closer inspection reveals subtle changes in the relative intensities of the diffraction peaks. Specifically, while the (110) peak at 14.1° remains the dominant reflection in both cases, its intensity relative to the (220) peak at 28.4° shifts from $\approx 2.6:1$ in the pristine film to $2.2:1$ after H_2 exposure, indicating a $\approx 15\%$ decrease in this peak ratio. Similarly, the (310)/(110) intensity ratio changes from ≈ 0.85 to ≈ 1.05 , reflecting a relative increase in higher-order reflections post-exposure. These changes in peak intensity ratios suggest a modification in the preferred orientation of the crystalline grains, rather than any bulk structural transformation. Such reorganization may result from surface-level interactions between hydrogen molecules and MAPI grain boundaries or defect-rich crystallographic planes, possibly mediated by hydrogen adsorption or shallow trap passivation. Given the reversibility of the optical (PL) response and the unchanged peak positions, these intensity ratio shifts likely reflect subtle reorientation or strain relaxation effects at the microstructural level,^[51] which are non-destructive but detectable.

To probe whether the optical response is governed solely by surface effects or includes bulk contributions, we compared the PL response of MAPI films with two different thicknesses. As shown in **Figure 6C**, the 800 nm film displays a significantly stronger PL modulation upon H_2 exposure than the 500 nm one. This indicates that the effect of H_2 on MAPI is not confined to surface interactions alone but likely involves diffusion into the film and modulation of bulk defect or trap states. We also examined how change in halide composition influence the sensing response and found that PL response of a mixed-halide film ($MAPbCl_xI_{3-x}$) upon H_2 exposure is notably reduced compared to the PL modulation observed in pure MAPI films (**Figure S2**, Supporting Information). This suppression in the PL response supports the idea that iodide vacancies or iodide-mediated defect states may play a key role in the sensing mechanism.

2.5. Trap Dynamics and Sensing Mechanism

Across all measurements, the characteristic signature involves a rapid increase in PL intensity followed by a decay below baseline during prolonged exposure, with partial recovery upon reintroduction of ambient air. This biphasic PL evolution implies a two-stage modulation of trap populations: initial passivation of shallow traps and subsequent activation of deeper, possibly bulk-localized, defect states.

The initial intensity spike upon H_2 introduction is consistent with the passivation of surface-related non-radiative recombination centers,^[32,33] likely iodide vacancies,^[34,35] by physisorbed H_2 . When neutralized, these shallow traps reduce non-radiative losses and temporarily increase radiative efficiency, as supported by spatial PL maps in **Figure 4**, showing localized intensity en-

hancements and modest wavelength blueshifts under H₂ flow. Additionally, Figure 2 (and its inset) highlights the immediacy of this PL enhancement, further reinforcing the rapid surface-level interaction. Critically, control measurements performed on encapsulated MAPI films (Figure 1D) show no response to hydrogen exposure, confirming that the PL modulation requires direct access of H₂ molecules to the perovskite surface and is not an artifact of gas flow, pressure fluctuation, or optical alignment. As exposure continues, the PL intensity decays below the original baseline. TRPL data in Figure 4 and the associated decay parameter distributions (Figures S4 and S5, Supporting Information) reveal an increase in the longer-lived recombination component (τ_2) across the mapped region. These findings indicate that H₂ penetrates into the film and perturbs deeper trap states, which could be vacancy clusters^[34,35] or undercoordinated Pb-I antisite defects,^[49] leading to enhanced non-radiative recombination and long-lived carrier trapping. The incomplete reversibility of these parameters following H₂ removal suggests the formation of a partially modified defect landscape resulting from H₂ exposure.

The data from mixed-halide films (Figure S2, Supporting Information) further support this interpretation. PL response to H₂ was observed in MAPbCl_xI_{3-x} films, but it was very subdued compared to that in MAPI. This variation suggests that the halide composition modulates trap energetics and hydrogen-accessible sites, consistent with a mechanism driven by defect interactions rather than redox chemistry or catalysis. The mixed-halide data thus extend the mechanistic framework to broader perovskite compositions and reinforce the role of lattice defects and surface chemistry in dictating sensor behavior. Importantly, XRD analysis confirms that no new crystalline phases or structural degradation occur during hydrogen exposure. Subtle changes in relative peak intensities suggest possible microstructural relaxation,^[51] but not decomposition. This rules out mechanisms based on hydrogen-induced chemical transformation, such as halide loss or lead metal formation. Furthermore, the lack of any response in encapsulated films (Figure 1D) excludes contributions from environmental light scattering or substrate effects.

Taken together, these observations establish that the hydrogen sensing mechanism in MAPI is best described as a reversible modulation of shallow and deep trap states via hydrogen adsorption and diffusion. The surface interactions passivate non-radiative sites, enhancing PL, while deeper diffusion perturbs long-lived traps that suppress emission. The spatial and kinetic heterogeneity seen across the film further suggests local variation in trap distributions and hydrogen accessibility, consistent with known grain boundary effects in polycrystalline perovskites.^[49] This mechanism is distinct from electrochemical or catalytic hydrogen sensors, as it does not require applied bias, metal interfaces, or irreversible reactions. Instead, it leverages the unique photophysical sensitivity of MHPs to defect population changes, offering a new optical modality for chemical sensing based purely on trap-state dynamics.

3. Conclusion

This study demonstrates that MAPI thin films function as rapid, room-temperature optical sensors for H₂ gas, exhibiting consistent, concentration-sensitive optical modulation. The sensing response is driven by reversible trap-state interactions rather than

chemical decomposition, as confirmed by crystallographic stability and control measurements. Using a combination of steady-state, spatially resolved, and time-resolved PL techniques, we reveal a biphasic mechanism involving initial passivation of shallow traps followed by slower interactions with deeper trap states. Importantly, these films operate without electrical bias and respond within seconds, offering a passive, contactless sensing platform suitable for critical applications such as aerospace fuel lines and cryogenic hydrogen storage systems. Their compatibility with fiber optics and remote interrogation systems further enhances their deployment potential in hazardous or inaccessible environments.

While some limitations remain, including partial reversibility in deep trap recovery and a gradual decline in baseline PL over repeated cycles, our data suggest that these effects are primarily due to subtle defect-state modulation rather than irreversible damage. Notably, measurements were carried out under ambient conditions spanning nearly a year, during which relative humidity varied from 20% to 90% (Table S2, Supporting Information). Despite the known sensitivity of MAPI to moisture, we observed consistent optical behavior across this range and no detectable structural degradation. This resilience, together with the demonstrated thermal stability during extreme cycling in space environments, positions it as a surprisingly robust material platform given its reputation for fragility.

Future work focused on surface passivation, incorporation of mixed-cation or all-inorganic MHPs, and gas-permeable encapsulation strategies will be essential to enhance environmental stability and reversibility. With continued materials engineering and integration advances, MAPI-based optical sensors have strong potential to meet the growing demand for low-power, high-resolution hydrogen detection across a range of challenging operational settings.

4. Experimental Section

Chemicals: Methylammonium iodide (MAI, ≥99%, Sigma-Aldrich), lead iodide (PbI₂, 99%, Sigma-Aldrich), N-methyl-2-pyrrolidone (NMP, 99.5%, Sigma-Aldrich), dimethyl sulfoxide (DMSO, ≥99.9%, Sigma-Aldrich), N,N-dimethylformamide (DMF, 99.8%, Sigma-Aldrich), and perovskite precursor ink (Perovskite Precursor Ink for Air Processing, Ossila) were used as purchased without any further purification. The perovskite precursor ink consisted of 3:1 methylammonium iodide to lead chloride in dimethylformamide.

Fabrication: MAPI ink was prepared in a glove box by mixing 0.636 g of MAI with 1.844 g of PbI₂ in a glass container, followed by 68 μL of NMP, 232 μL of DMSO, and 3 mL of DMF. The ink was left to mix at 60 °C overnight. MAPI thin films were fabricated by depositing 40 μL of MAPI ink on glass substrates, followed by spin-coating at 2000 rpm for 60 s. The films were then annealed at 90 °C for 5 min on a hotplate. Mixed halide perovskite thin films were fabricated by depositing 50 μL of perovskite precursor ink on glass substrates, followed by spin-coating at 3000 rpm for 30 s. The films were then annealed at 90 °C for 35 min on a hotplate.

Photoluminescence Spectroscopy: Thin films were excited with a continuous wave 409 nm laser light (Coherent Cube Diode Laser System) focused using a plano-convex lens. Light emitted by the sample was filtered by a 450 nm longpass filter before being collected by the spectrometer (OceanOptics USB4000).

Gas Control System: Measurements were performed by placing the thin films in a gas cell with a transparent broadband window. The H₂ flow was controlled by a flow meter to ensure flow rates were held at 3 L min⁻¹.

For concentration measurements, N₂ and H₂ were mixed with 2 separate flow meters to control concentration, which fed into a third flow meter that restricted the total gas flow to 3 L min⁻¹.

Time-Resolved Photoluminescence Spectroscopy: For time-resolved photoluminescence (TRPL) spectroscopy, a pulsed supercontinuum source (NKT Photonics) was tuned to 430 nm at a repetition rate of 76 MHz for excitation. The emission from the films was directed to single-photon avalanche diodes that connect to a time-correlated single-photon counting system (PicoQuant). The films were exposed to H₂ prior to excitation, and the gas cell remained sealed for the entirety of the measurement. For every TRPL curve the PL intensity is fit to a bi-exponential fit: $I_{PL} = A_1 \exp(-t/\tau_1) + A_2 \exp(-t/\tau_2)$, where τ_1 and τ_2 are the fast and slow time scales, respectively, representing two different routes for recombination. From the fit, an average lifetime τ is calculated as follows: $\tau = A_1 \tau_1^2 + A_2 \tau_2^2 / (A_1 \tau_1 + A_2 \tau_2)$. Additionally, the contribution of each of the recombination routes is represented as $C_i = A_i \tau_i / \sum A_i \tau_i$.

X-Ray Diffraction: The x-ray diffraction (XRD) data was taken using a PANalytical X'Pert PRO Theta/Theta Powder X-ray Diffraction system.

Confocal Microscopy: The confocal data was taken using a LSM880 confocal microscope. The films were excited using a 405 nm laser and the emission was taken by filtering light between 708 and 759 nm.

Supporting Information

Supporting Information is available from the Wiley Online Library or from the author.

Acknowledgements

This work was supported in part by funding from the National Science Foundation award DGE-2125510.

Conflict of Interest

The authors declare no conflict of interest.

Data Availability Statement

The data that support the findings of this study are available from the corresponding author upon reasonable request.

Keywords

gas sensing, hydrogen gas, metal halide perovskite, photoluminescence

Received: June 2, 2025
Revised: August 5, 2025
Published online:

- [1] P. S. Chauhan, S. Bhattacharya, *Int. J. Hydrogen Energy* **2019**, *44*, 26076.
- [2] S. Okazaki, H. Nakagawa, S. Asakura, Y. Tomiuchi, N. Tsuji, H. Murayama, M. Washiya, *Sens. Actuat. B* **2003**, *93*, 142.
- [3] U. S. Energy Information Administration. Production of Hydrogen, <https://www.eia.gov/energyexplained/hydrogen/production-of-hydrogen.php>, **2024**.
- [4] The Royal Society, The Role of Hydrogen and Ammonia in Meeting the Net Zero Challenge **2021**.
- [5] U. S. Department of Energy, Hydrogen Fuel Basics, <https://www.energy.gov/eere/fuelcells/hydrogen-fuel-basics>, **2024**.
- [6] N. L. Panwar, S. C. Kaushik, S. Kothari, *Renew. Sustainable Energy Rev.* **2011**, *15*, 1513.
- [7] Y. Li, Z. Wang, X. Shi, R. Fan, *Process Saf. Environ. Protect.* **2023**, *171*, 619.
- [8] Z. Zhang, M. Shang, *Sci. Rep.* **2024**, *14*, 3363.
- [9] U.S. Department of Energy, Hydrogen Storage, <https://www.energy.gov/eere/fuelcells/hydrogen-storage>, **2025**.
- [10] S. M. Aceves, F. Espinosa-Loza, E. Ledesma-Orozco, T. O. Ross, A. H. Weisberg, T. C. Brunner, O. Kircher, *Int. J. Hydrogen Energy* **2010**, *35*, 1219.
- [11] N. Yang, J. Deng, C. Wang, Z. Bai, J. Qu, *Int. J. Hydrogen Energy* **2024**, *50*, 1029.
- [12] T. Hübert, L. Boon-Brett, G. Black, U. Banach, *Sens. Actuat. B* **2011**, *157*, 329.
- [13] M. Grätzel, *Nat. Mater.* **2014**, *13*, 838.
- [14] S. A. Olaleru, J. K. Kirui, D. Wamwangi, K. T. Roro, B. Mwakikunga, *Sol. Energy* **2020**, *196*, 295.
- [15] J. S. Manser, J. A. Christians, P. V. Kamat, *Chem. Rev.* **2016**, *116*, 12956.
- [16] G. Xing, N. Mathews, S. S. Lim, N. Yantara, X. Liu, D. Sabba, M. Grätzel, S. Mhaisalkar, T. C. Sum, *Nat. Mater.* **2014**, *13*, 476.
- [17] D. W. de Quillettes, S. M. Vorpahl, S. D. Stranks, H. Nagaoka, G. E. Eperon, M. E. Ziffer, H. J. Snaith, D. S. Ginger, *Science* **2015**, *348*, 683.
- [18] National Renewable Energy Laboratory, Best Research-Cell Efficiency Chart, <https://www.nrel.gov/pv/cell-efficiency.html>, **2023**.
- [19] H. S. Jung, N.-G. Park, *Small* **2015**, *11*, 10.
- [20] H. C. Wang, Z. Bao, H. Y. Tsai, A. C. Tang, R. S. Liu, *Small* **2018**, *14*, 1702433.
- [21] A. Maity, S. Mitra, C. Das, S. Siraj, A. K. Raychaudhuri, B. Ghosh, *Mater. Res. Bull.* **2021**, *136*, 111142.
- [22] S. Ruan, J. Lu, N. Pai, H. Ebendorff-Heidepriem, Y.-B. Cheng, Y. Ruan, C. R. McNeill, *J. Mater. Chem. C* **2018**, *6*, 6988.
- [23] H. Huang, M. Hao, Y. Song, S. Dang, X. Liu, Q. Dong, *Small* **2020**, *16*, 1904462.
- [24] X. Fu, S. Jiao, N. Dong, G. Lian, T. Zhao, S. Lv, Q. Wang, D. Cui, *RSC Adv.* **2017**, *8*, 390.
- [25] Z. Weng, J. Qin, A. Umar, J. Wang, X. Zhang, H. Wang, X. Cui, X. Li, L. Zheng, Y. Zhan, *Adv. Funct. Mater.* **2019**, *29*, 1902234.
- [26] Z. Zhang, J. Yi, H. Han, Y. Meng, H. Zhang, Y. Jiang, *ACS Appl. Mater. Interfaces* **2022**, *14*, 33580.
- [27] E. Gagaoudakis, A. Panagiotopoulos, T. Maksudov, M. Moschogiannaki, D. Katerinopoulou, G. Kakavelakis, G. Kiriakidis, V. Binas, E. Kymakis, K. Petridis, *J. Phys. Mater.* **2020**, *3*, 014010.
- [28] J.-W. Lee, S.-G. Kim, J.-M. Yang, Y. Yang, N.-G. Park, *APL Mater.* **2019**, *7*, 041111.
- [29] C. C. Boyd, R. Cheacharoen, T. Leijtens, M. D. McGehee, *Chem. Rev.* **2019**, *119*, 3418.
- [30] M. Lepore, I. Delfino, *Sensors* **2022**, *22*, 7905.
- [31] J. Arteaga, V. Cherrette, J. Z. Zhang, S. Ghosh, *J. Phys. Chem. C* **2023**, *127*, 17836.
- [32] C. M. Wolff, P. Caprioglio, M. Stolterfoht, D. Neher, *Adv. Mater.* **2019**, *31*, 1902762.
- [33] L. Hu, L. Duan, Y. Yao, W. Chen, Z. Zhou, C. Cazorla, C. Lin, X. Guan, X. Geng, F. Wang, T. Wan, S. Wu, S. Cheong, R. D. Tilley, S. Liu, J. Yuan, D. Chu, T. Wu, S. Huang, *Adv. Sci.* **2022**, *9*, 2102258.
- [34] Y. Liang, X. Cui, F. Li, C. Stampfl, S. P. Ringer, J. Huang, R. Zheng, *Sol. RRL* **2022**, *6*, 2200211.
- [35] X. Zhang, J.-X. Shen, M. E. Turiansky, C. G. Van De Walle, *Nat. Mater.* **2021**, *20*, 971.
- [36] S. Masuzawa, S. Okazaki, Y. Maru, T. Mizutani, *Sens. Actuat. B* **2015**, *217*, 151.

- [37] A. Harley-Trochimczyk, J. Chang, Q. Zhou, J. Dong, T. Pham, M. A. Worsley, R. Maboudian, A. Zettl, W. Mickelson, *Sens. Actuat. B* **2015**, 206, 399.
- [38] G. Korotcenkov, S. D. Han, J. R. Stetter, *Chem. Rev.* **2009**, 109, 1402.
- [39] C. Ramesh, N. Murugesan, M. V. Krishnaiah, V. Ganesan, G. Periaswami, *J. Solid State Electrochem.* **2008**, 12, 1109.
- [40] C. Wagner, *J. Chem. Phys.* **1950**, 18, 69.
- [41] A. Sanger, A. Kumar, A. Kumar, R. Chandra, *Sens. Actuat. B* **2016**, 234, 8.
- [42] L. Boon-Brett, J. Bousek, P. Castello, O. Salyk, F. Harskamp, L. Aldea, F. Tinaut, *Int. J. Hydrogen Energy* **2008**, 33, 7648.
- [43] L. Boon-Brett, J. Bousek, P. Moretto, *Int. J. Hydrogen Energy* **2009**, 34, 562.
- [44] D. Iannuzzi, M. Slaman, J. H. Rector, H. Schreuders, S. Deladi, M. C. Elwenspoek, *Sens. Actuat. B* **2007**, 121, 706.
- [45] D. R. Baslet, B. Fruhberger, E. Klaassen, S. Cemalovic, C. L. Britton Jr., S. V. Patel, T. E. Mlsna, D. McCorkle, B. Warmack, *Sens. Actuat. B* **2003**, 88, 120.
- [46] A. M. Bothwell, C. L. Reich, A. H. Danielson, A. Onno, Z. C. Holman, W. S. Sampath, D. Kuciauskas, *Sol. RRL* **2023**, 7, 2201029.
- [47] A. Choundhury, R. K. Gupta, R. Garai, P. K. Iyer, *Adv. Mater. Interfaces* **2021**, 8, 2100574.
- [48] E. V. Péan, S. Dimitrov, C. S. De Castro, M. L. Davies, *Phys. Chem. Chem. Phys.* **2020**, 22, 28345.
- [49] Z. Fang, J. Sun, S. Liu, L. Ding, *J. Semicond.* **2023**, 44, 080201.
- [50] F. Brivio, J. M. Frost, J. M. Skelton, A. J. Jackson, O. J. Weber, M. T. Weller, A. R. Goñi, A. M. A. Leguy, P. R. F. Barnes, A. Walsh, *Phys. Rev. B* **2015**, 92, 144308.
- [51] Y. Yalcinkaya, I. M. Hermes, T. Seewald, K. Amann-Winkel, L. Veith, L. Schmidt-Mende, S. A. L. Weber, *Adv. Energy Mat.* **2022**, 12, 2202442.